Grid-Based Imaging of X-rays and Gamma Rays with High Angular Resolution

Pascal Saint-Hilaire, Albert Y. Shih, Gordon J. Hurford,
and Brian Dennis

Contents

P. Saint-Hilaire (✉) · G. Hurford
Space Sciences Laboratory, University of California Berkeley, Berkeley, CA, USA
e-mail: pascal@ssl.berkeley.edu; shilaire@ssl.berkeley.edu; ghurford@berkeley.edu

A. Shih · B. Dennis
Solar Physics Laboratory, Goddard Space Flight Center, Greenbelt, MD, USA
e-mail: albert.y.shih@nasa.gov; brian.r.dennis@nasa.gov; brdennis@comcast.net

C. Bambi, A. Santangelo (eds.), *Handbook of X-ray and Gamma-ray Astrophysics*,
https://doi.org/10.1007/978-981-16-4544-0_170-1

Abstract

This chapter contains an overview of the basic principles of X-ray and gamma-ray imaging for astronomy that achieve high angular resolution with non-focusing optics. Specific topics include systems with single-grid masks, with pairs of grids known as bi-grid collimators, and with more than two grids known as multi-grid collimators. A discussion of each type is given along with advantages and limitations of the various design options and descriptions of actual implementations.

Keywords

X-ray · Gamma ray · Imaging · Grid · Collimator · Solar flare

Introduction

At most wavelengths, imaging is based on optics that use reflection from a curved mirror or refraction through a lens to focus the incident light onto a multielement detector. This provides a direct image of the source. However, at very short wavelengths ($\leq$0.1 nm, equivalent to photon energies $\geq$10 keV), the physics of reflection or refraction can render such direct imaging impractical so that other techniques must be employed for hard X-rays and gamma rays (e.g., Ramsey et al., 1993; Bradt et al., 1968, 1992). This is particularly true for imaging with high angular resolution (few arcsecs or less) and/or over a large ($\geq 1^\circ$) field of view (FOV), both of which are critical for solar flare observations. For imaging at shorter wavelengths than is currently possible with focusing optics, it is necessary to resort to collimators, masks, and/or grids that provide an imaging capability by using absorption or scattering rather than reflection or refraction. They are used to selectively block or transmit the incident flux depending on the arrival direction of the photons. This can effectively transform the information about the angular distribution of the incident radiation into either a spatial variation or a temporal variation in the detected photon flux, i.e., they produce spatial or temporal modulation. Such systems are implemented as a single absorbing layer with apertures (mask), a pair of separated grids (bi-grid collimator), or multiple grids (multi-grid collimator).

A related approach uses so-called Söller collimators (Soller, 1924) that consist of a set of continuous blades, each oriented parallel to the desired direction of photon travel so as to restrict the photon transmission to a limited range of angles. Such collimators can be scanned across the field of view to provide limited angular resolution, but they are currently seldom used for solar X-ray or gamma-ray imaging, so we will not consider them further here. They are useful, however, for coarsely constraining the FOV (e.g., to limit background).

Configurations of collimator-based imagers are quite diverse, and many are adaptable to a wide range of spacecraft constraints. The choice of collimation approach – whether to use a single mask, a bi-grid, or a multi-grid collimator, and whether to use temporal or spatial modulation – depends on various design drivers. These include the available mass, volume, and possible collimator length; the type of spacecraft attitude control (three-axis or spin stabilized); the detector characteristics (particularly the spatial resolution and energy range and resolution); and the relative scientific importance of angular and temporal resolution, FOV, and sensitivity.

In this chapter, we will primarily review grid-based imaging in X-rays and gamma rays as used for solar flare observations. Solar imaging can have very different requirements than other astrophysical targets. Solar flares cover a wide range of intensities with the strongest being much more intense than other astrophysical sources. They are relatively short-lived with durations of minutes to hours and variations on timescales down to sub-seconds. They require coverage of spatial scales from an arcsec to a few arcmin over a $\sim 1^\circ$ FOV to image a flare at any location on the visible side of the Sun.

In the following sections, we discuss the different types of systems in their historical order and conclude with a color-coded summary table and a referenced list of past missions that used the various architectures.

Multi-Grid Collimators

Generalities

A set of collimators, each pointing in a slightly different direction, and terminated by a detector element (pixel) independent of the others can be realized with a multi-grid system. As depicted in Fig. 1, a pair of grids modulates into a series of peaks the transmission of a point source as function of its position across the field of view. Inserting additional grids suppresses the response at intermediate peaks. If enough additional grids are inserted, this can provide a system that has only one response peak across the FOV. A single such collimator can be rastered in time, or a fixed array of such collimators can be employed, each with its peak response in a (slightly) different direction. In either case, the result is a direct imaging system, effectively equivalent to a conventional focused telescope in that it has multiple detector elements, each of which is sensitive to a specific area on the source. The angular resolution is determined by the pitch of the collimator grids.

The advantage over the indirect imaging provided by single-grid or bi-grid systems is that no image reconstruction is required and hence the signal from strong sources does not affect the detection of weak ones. A significant disadvantage, however, is that the available frontal area of the instrument must be divided among many small subcollimators, each with its own look direction. Alternatively, for scanned systems, a given source is observed with a low duty cycle, especially since the location of the source is usually not known a priori. In either case, the sensitivity to any given source in the FOV can be very low since only a small fraction of the time or area can be spent on observing the source of interest.

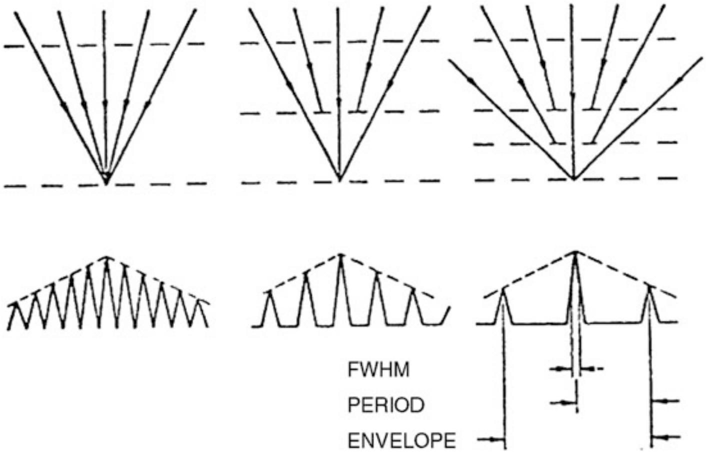

Fig. 1 Top: Possible photon paths for bi-grid and multiple grid collimators, illustrating the periodic maxima in their response and the effect of intermediate grids. Bottom: Corresponding plots of the effective area as a function of incident angle. For a given collimator length, the angular resolution is given by the ratio $\frac{1}{2}$ grid pitch/separation; the response envelope (FOV) is defined by the detector and grid size. The intermediate grids affect the period

Multi-Grid Example Application: HXIS on *SMM*

The Hard X-ray Imaging Spectrometer (HXIS) on the *Solar Maximum Mission* (*SMM*) (van Beek et al., 1980) is a good example of the mutli-grid approach (Figs. 2 and 3). It had $8''$ (over a $160''$ FOV) and $32''$ (over a $6.6'$ FOV) pixels. There is a priori no limitations to the FOV covered, although the number of "collimators" can get prohibitively large. For example, to cover a 1° (twice the solar diameter) circular angular area with $8''$ pixels, more than 10^5 equivalent collimators would be needed.

Bi-grid Systems: Fourier Imagers

Generalities

A bi-grid modulation collimator (Oda, 1965) consists of two separated grids. Each grid consists of a large number of parallel slats that are opaque to the photons to be imaged (X-rays or gamma rays), while the slits between the slats are transparent to these photons. This provides a way to decouple the achievable imaging angular resolution from the spatial resolution of the detector placed behind the collimator to measure the modulated photon flux transmitted by the two grids.

Bi-grid collimators fall into two broad classes: those that generate a spatial pattern in the transmitted photon flux that depends on the incident direction (spatial modulation) and those that impose a distinctive time dependence on the transmitted

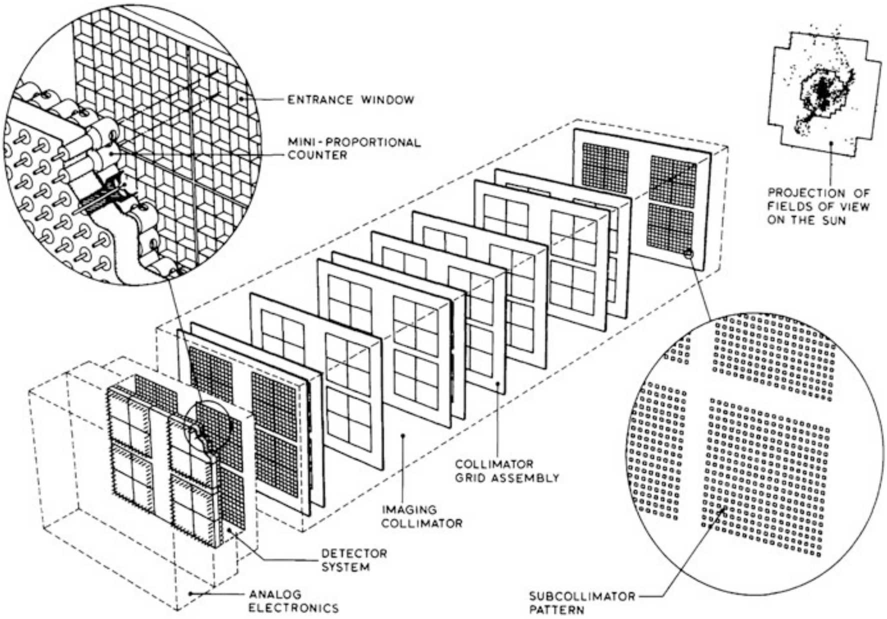

Fig. 2 The HXIS instrument on *SMM*. The collimator contains ten grid plates, each divided into sections as indicated on plates 1 and 10. Each plate carries four grids. The images formed are analyzed by the position-sensitive detector system containing in total 900 mini-proportional counters. (Reproduced from van Beek et al. (1980) with permission from Frank Van Beek)

photon flux (temporal modulation). In the former case, the detector must have only sufficient spatial resolution to measure the spatial pattern, whereas in the latter case, no spatial resolution is required at all. In both cases, the use of bi-grid modulation collimators opens the way to obtaining much higher angular resolution within a given instrument envelope than would otherwise be possible with current detector technology.

In a bi-grid collimator using spatial modulation (sometimes called an imaging collimator), the pitch *and* orientation of the front and rear grids differ by small amounts so that they have slightly different spatial frequencies. As a result, for a given direction of incidence, the transmitted flux forms a large-scale Moiré pattern that has one or a few cycles across the detector as shown in Fig. 4a and b. The phase of this Moiré pattern (i.e., the location of its maximum) depends sensitively (and periodically) on the incident photon direction. It goes through a complete cycle with a change of photon direction given by the ratio of the average grid pitch to the separation between the two grids. Although the Moiré pattern really consists of a large number of narrow stripes (corresponding to the grid pitch), it can be characterized by a detector whose spatial resolution needs to be good enough to see only its large-scale “envelope.” Therefore, the spatial resolution requirement on the detector is determined by the grid diameter (*Solar Orbiter*’s STIX uses effectively

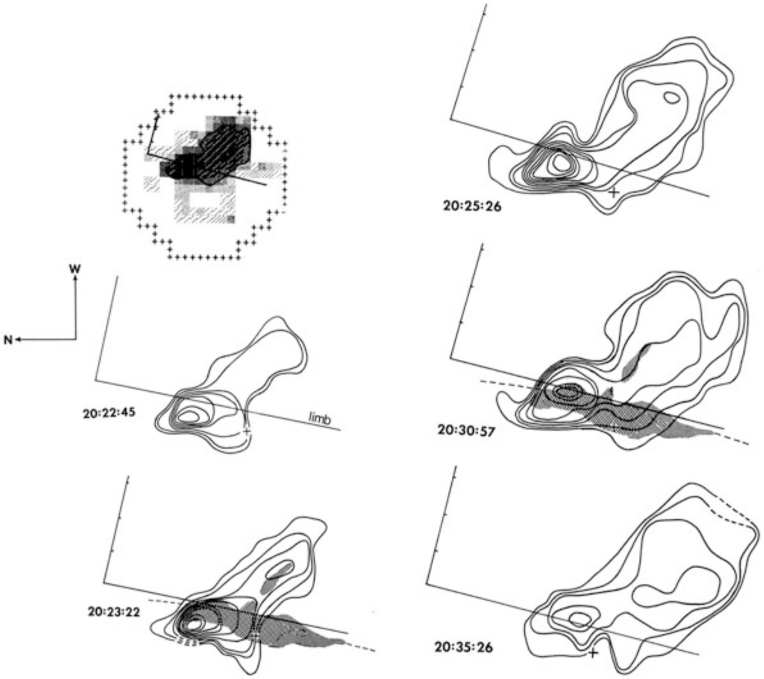

Fig. 3 Contour plots of the 1980 April 30 limb flare observed by *SMM*/HXIS at energies between 3.5 and 8 keV. An Hα overlay (*shaded area*) is shown in two of the images. The shading of the HXIS image, top left (small scale), is proportional to the count rate in each 8″ × 8″ elements. The solar limb is indicated, with the corona above and the disk below. (Reproduced from van Beek et al. (1981) with permission from Frank Van Beek)

only four pixels for each subcollimator), while the angular response of the collimator as a whole is determined by the much smaller grid pitch.

Alternatively, in a time-modulation collimator, the top and bottom grids have identical pitch and orientation as shown in Fig. 4c and d. If the photon direction with respect to the collimator changes as a function of time, the total transmitted flux also varies with time. The angular period of this transmitted flux is given by the ratio of the grid pitch to the distance between the two grids, and the FWHM angular resolution is just half this period. Such time variations can be measured with a detector that need not have any spatial resolution whatsoever, and so it can be chosen or optimized on the basis of other considerations such as spectral resolution or high-energy response.

It has been shown (Makishima et al., 1977; Prince et al., 1988) that the amplitude and phase of the primary sinusoidal component of one of the quasi-triangular patterns seen in Fig. 5 provide a direct measurement of a single Fourier component of the source angular distribution. Thus, the response of a bi-grid collimator is a precise mathematical analogue to that of a pair of antennas in a radio interferometer, whose correlated signal also measures one such Fourier component. In both the

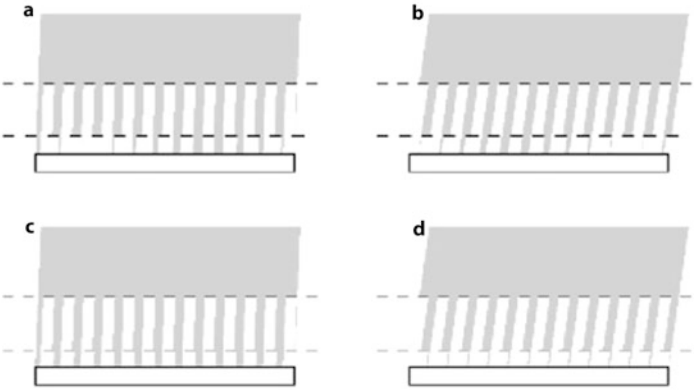

Fig. 4 Schematic illustration of the transmission of two types of bi-grid collimators. Panels (**a**) and (**b**) show a system that produces spatial modulation of the incident flux. This is achieved by making the front and rear grids with slightly different pitch. For the two incident beam directions shown, the total transmitted flux is about the same, but the location on the detector of the maximum transmission is significantly shifted. Alternatively, panels c and d show a system that produces temporal modulation of the incident flux as the direction to the source is changed. In this case, the grid pitches are identical, but changing the incident direction changes the total detected flux

X-ray/gamma-ray and radio cases, images can be reconstructed from a set of Fourier component measurements made at a large number of angular frequencies. This perspective on the response of a bi-grid collimator greatly simplifies analyses of its angular response.

Useful insights into the response of a bi-grid collimator can be gained by considering the link between its transmission as a function of time (or position for an imaging collimator) and its transmission as a function of incident photon direction. If the slits and slats of the grids are of equal width, then this dependence has a quasi-triangular form. For the case of a rotating collimator, Fig. 5 shows the modulation as a function of time and grid phase, along with their harmonic (Fourier) decomposition, and for three slit-to-pitch (s/p) ratios. Due to the nonzero thickness of the slats, the *effective* s/p can vary as a function of angular offset of the source from the collimator axis (see Fig. 6 for the *RHESSI* case). The harmonic decomposition of the transmission is displayed in Fig. 7 as a function of this effective s/p.

For a point source, the amplitude of the modulation pattern is proportional to the source intensity, and the timing (or location in the case of spatial modulation) of the transmission maximum depends on the source direction. Note that there is no information contained in the period since that is determined by the collimator's design and/or its changing orientation with respect to the source. The Fourier series decomposition of the modulation profile in Fig. 5 showcases the fact that information about angular resolutions at integer multiples of the fundamental subcollimator (SC) FWHM exist, albeit at poorer signal to noise, and can also be exploited in the imaging process.

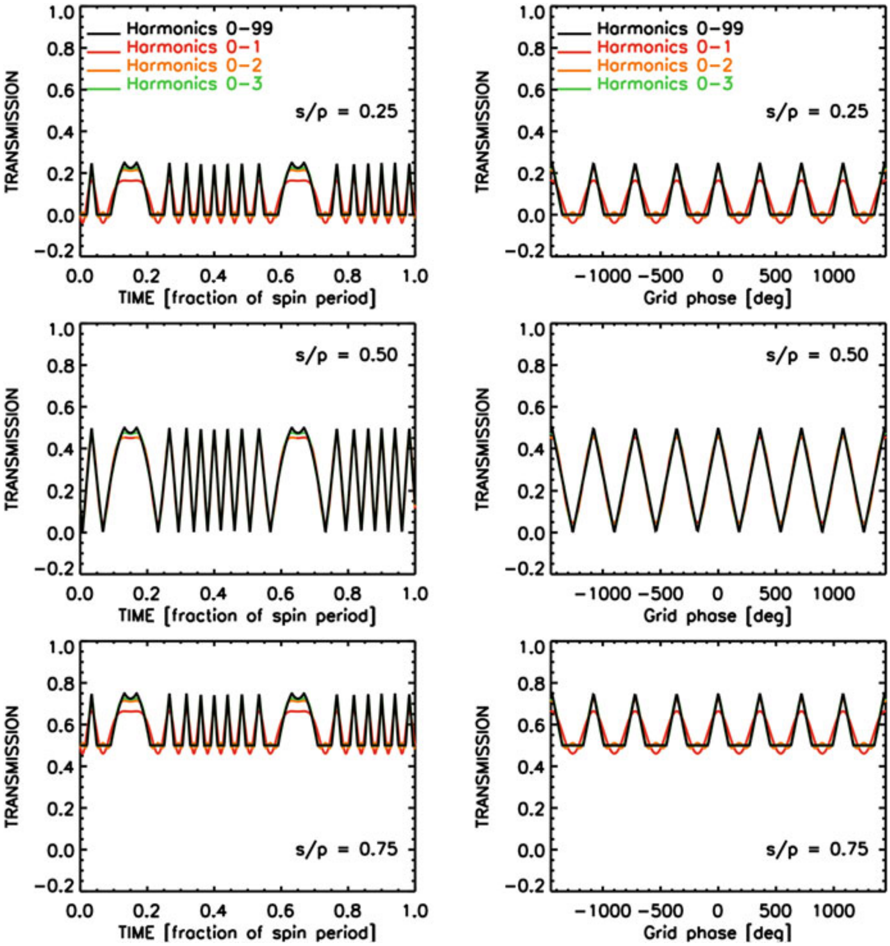

Fig. 5 Illustration of the time variation over one rotation period of the transmission of the radiation from a point source at infinity through a bi-grid collimator with effective slit-to-pitch ratios of 0.25, 0.5, and 0.75, mounted on a spinning spacecraft. The variations in the period of the modulation arise since, in the plane orthogonal to the grid slits, the source apparently moves with simple harmonic motion (the grid phase is $\Phi = 2\pi\rho\cos(\omega t - \alpha)$, where ρ (here, $\rho = 4$) is the angular offset of the source with respect to the collimator imaging axis in fractions of the grid's angular pitch p/L, $\omega = 2\pi/T$ where T is the collimator spin period and α is the grid's reference orientation about the imaging axis. For simplicity, spin axis and imaging axis were here assumed the same, and the thin-grid approximation was used (s/p constant throughout the FOV), but that is not generally the case. Decomposition of the transmission profile into its first few Fourier series terms is also shown (colored lines). They can have negative values

At this point, it is useful to introduce the concept of "visibilities" borrowed from radio astronomy. Their application in the context of bi-grid collimators is explained in the (Hurford et al., 2002) appendix. (See also the *RHESSI* Science Nugget #39

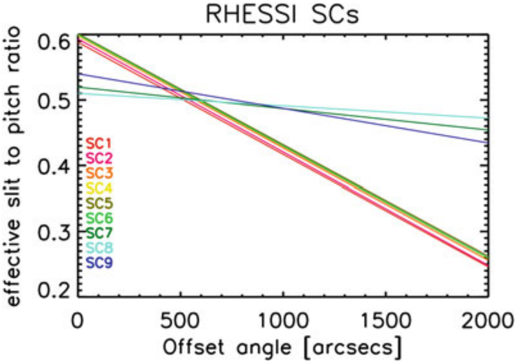

Fig. 6 *RHESSI* effective slit-to-pitch ratio as a function of angular offset from the grid (imaging) axis, due to the shadowing created by the slats' thickness. The geometric approximation presented here is valid at low energies, but should be corrected at gamma-ray energies for the effective thickness of the slats. At a nonzero incidence angle, the photon path may cross only a small corner of a rectangular slat. This would still block low-energy X-rays but only a fraction of the high-energy gamma rays. Note that for *RHESSI*, subcollimators 6 & 9 were chosen to be thick enough to block gamma rays. SC 8 had the widest field of view but could block photons only at energies below ~700 keV

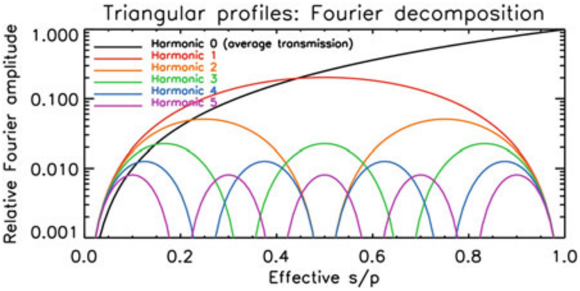

Fig. 7 Fourier series decomposition of the bi-grid transmission as a function of slit-to-pitch ratio s/p

available from https://hesperia.gsfc.nasa.gov/rhessi3/news-and-resources/results/nuggets/.) Roughly speaking, a visibility is a complex number that contains the amplitude (provided by the detectors) and phase (provided by the aspect system) of a particular Fourier spatial component of the source region. It includes all corrections for pointing excursions, transmission variations, and detector sensitivity effects. Thus, the inverse Fourier transform produces a "dirty map" of the source with most of the instrumental artifacts removed.

Although a time-modulation collimator can use a simpler detector system with limited, or even no, spatial resolution, some provision must be made to continually move the collimator with respect to the source so as to change the relative direction of the incident photons. This can be done by mechanically rocking the collimator, or by exploiting random motions (as with an unstably pointed balloon platform). However, a common approach is to mount the collimator on a rotating spacecraft to form a rotating modulation collimator (RMC; Schnopper et al., 1968). As the collimator rotates, its response over a limited range of angles is quasiperiodic as shown in Fig. 5. Over a half-rotation, the amplitude and phase of the modulation measure a set of Fourier components at a complete set of orientations at the spatial frequency determined by the grid pitch and separation. In the parlance of radio interferometry, the system measures spatial frequencies in a circle in the uv (spatial frequency) plane in analogy to Earth rotation synthesis, except on a much more rapid timescale determined by the spacecraft rotation rate.

Early implementations of the rotating modulation collimator were used for surveys where the system detected point sources over a relatively wide FOV. Mertz (1967) also suggested using such collimators as imaging devices for extended sources. The most ambitious implementation to date of such an imager is *RHESSI* (Lin et al., 2002), which uses a set of nine RMCs to image extended solar flare X-ray and gamma-ray sources (Hurford et al., 2002), achieving angular resolutions as high as 2.3 arcsec. The effectiveness of multiple RMCs in characterizing extended sources is based on the fact that a bi-grid collimator cannot modulate X-rays from a source whose angular width is much larger than the collimator resolution. As a result, comparison of the modulation amplitude among collimators with different angular resolutions can provide a measurement of source size (e.g., Schmahl & Hurford 2002 and Fig. 8).

One measure of the performance of an RMC as an imager is the dynamic range of its images, i.e., the ratio of the brightest source in the FOV to the faintest credible feature. The dynamic range can be limited by any of three broad factors. First, a typical set of RMCs measures only a few dozen to a few hundred independent Fourier components, each of which is fully represented by a single complex number. Since the number of observables is so limited, there is an unavoidable limitation on the complexity of the images that can be reconstructed. Second, photon statistics can be a limitation in both astrophysical and solar observations. This translates directly into a statistical uncertainty in the measure of each Fourier component that again limits the achievable dynamic range. Third, as with any instrument, there are inevitable calibration uncertainties that constrain the accuracy of each measurement. In practice, the relative magnitude of these factors depends on the circumstances.

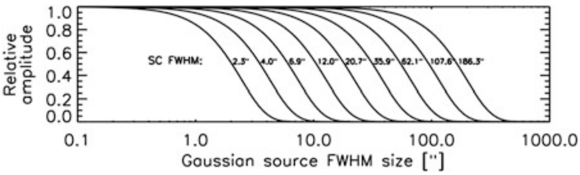

Fig. 8 Relative modulation amplitude for each of the nine *RHESSI* subcollimators as a function of the FWHM of a Gaussian source

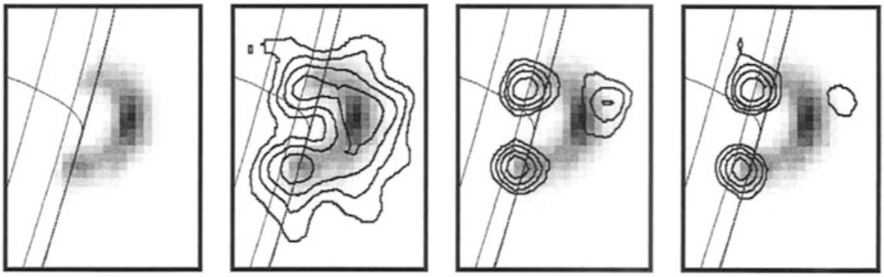

Fig. 9 Contour plots of *Yohkoh*/HXT images at different HXR energies overlaid on a *Yohkoh*/SXT SXR image. (Reproduced from Masuda (2002) with permission from S. Masuda)

Bi-grid Example Application: *Yohkoh*/HXT's and *ASO-S*/HXI's Fixed Subcollimators with Sine/Cosine Components

The Hard X-ray Telescope (HXT; Kosugi et al., 1991) on the Japanese *Yohkoh* mission, a 3-axis stabilized spacecraft, had 64 fixed bi-grid subcollimators of various pitches and orientations. It measured just 32 components covering spatial scales from 8 to 20″ (Fig. 9). China's Advanced Space-based Solar Observatory (ASO-S), launched in 2022, has a similar instrument, the Hard X-ray Imager (HXI Zhang et al., 2019), which has 91 subcollimators, including 1 without grids for total flux knowledge. With this approach, each spatial scale and orientation requires a "cosine" and "sine" subcollimator pair (cosine, slits of both grids are aligned; sine, slits of both grids have a relative alignment offset of a quarter of the grid pitch). Such pairings are not needed for STIX and *RHESSI* types of imaging (see next sections).

Bi-grid Example Application: *Solar Orbiter*/STIX's Fixed Subcollimators Using Moiré Patterns and Coarse Detectors

The *Solar Orbiter* mission carries an instrument (Fig. 10) called STIX, the Spectrometer Telescope for Imaging X-rays (Krucker et al., 2020) covering a 4–150 keV energy range. It is described in greater details in a separate chapter of this volume.

STIX has 30 imaging subcollimators whose front and rear grids have slightly different pitch and/or orientation to create moiré patterns projected on the surface of what is effectively a 4-pixel CZT detector (1 detector per SC), to measure 30 visibilities (Fig. 11) covering 10 angular scales (from ∼7″ to ∼3′) in several orientations. Some early results are displayed in Fig. 12.

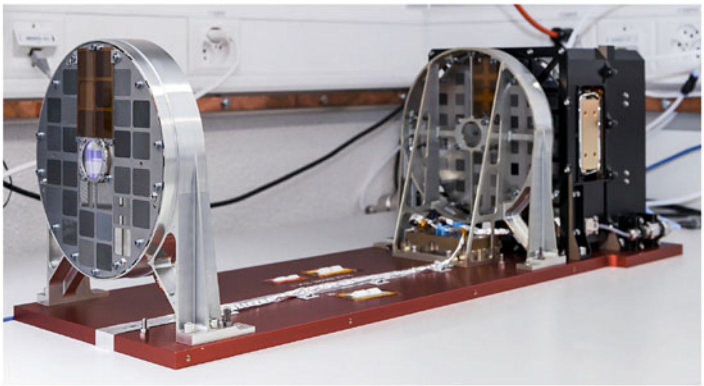

Fig. 10 Photographic view of the STIX instrument. (From Krucker et al. 2020)

Bi-grid Example Application: *RHESSI's* Rotating Modulation Collimators (RMCs)

RHESSI Design

A separate chapter of this book provides a detailed description of RHESSI and its scientific legacy. Here we provide an abbreviated account of its use of multiple bi-grid modulation collimators on a rotating spacecraft to provide high angular resolution imaging spectroscopy of both X-rays and gamma rays from solar flares.

RHESSI (Lin et al., 2002) was designed with the primary scientific objective of understanding particle acceleration (both electrons and ions) and explosive energy release in magnetized plasmas at the Sun. Previous X-ray measurements, coupled with measurements at other wavelengths, had shown that in order to achieve that goal for electron acceleration, hard X-ray imaging was required with an angular resolution in the few-arc-second range at energies from below 10 keV to several hundred keV. Such an angular resolution was necessary to separate chromospheric footpoint sources and distinguish them from the hot coronal sources, and to determine the spectra of the bremsstrahlung emission from nonthermal electrons at energies well above that of the thermal emission from plasma with temperatures ranging from below 10 MK to in excess of 50 MK. In addition, it was necessary to have an effective sensitive area of $\sim 100\,\mathrm{cm}^2$ in order to detect weaker events while also avoiding saturation for the largest events. This corresponds to a requirement for handling a dynamic range of some 10^5 in flare X-ray intensity from small GOES B-class events to the largest X10-class events. For RHESSI, this dynamic range was achieved by using two sets of aluminum attenuators that were automatically moved in front of the detectors to absorb an energy-dependent fraction of the incident flux when the total count rate exceeded $\sim 10^4$ counts s^{-1} detector^{-1} (Smith et al., 2002).

In order to achieve the goal of understanding ion acceleration, gamma-ray imaging and spectroscopy were required at energies between hundreds of keV to tens of MeV. At these energies, lines and continuum emission are produced

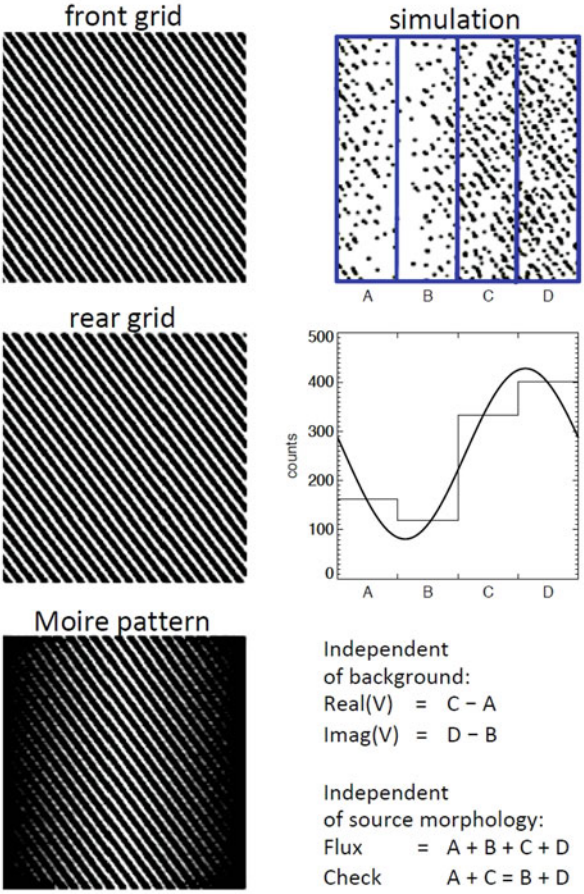

Fig. 11 STIX measurement of a visibility. Two panels on the top-left: front/rear pair of grids for one subcollimator. Close inspection shows that they have slightly different pitch and orientation. The combined transmission for an on-axis point source yields a moiré pattern (bottom-left panel). A simulation for an off-axis source shows the location of detected photons (top-right panel), as seen by a detector with four large pixels (blue). Accumulated counts in the four pixels are shown in the center-right panel. Differences among these counts (bottom right) yield the real and imaginary parts of the Fourier component independent of background. The sum over the four pixels yields the incident flux (plus background), independent of the visibility. There is also a cross-check that is independent of the visibility, flux, and background. (From Krucker et al. 2020)

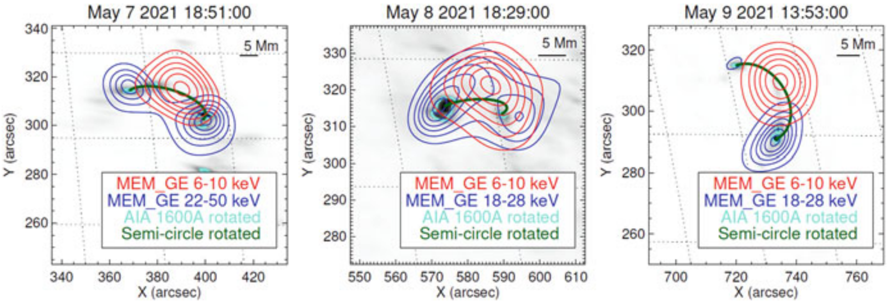

Fig. 12 *Solar Orbiter*/STIX contours overlaid on *Solar Dynamics Observatory*/AIA 1600 Å image. (From Massa et al. 2022)

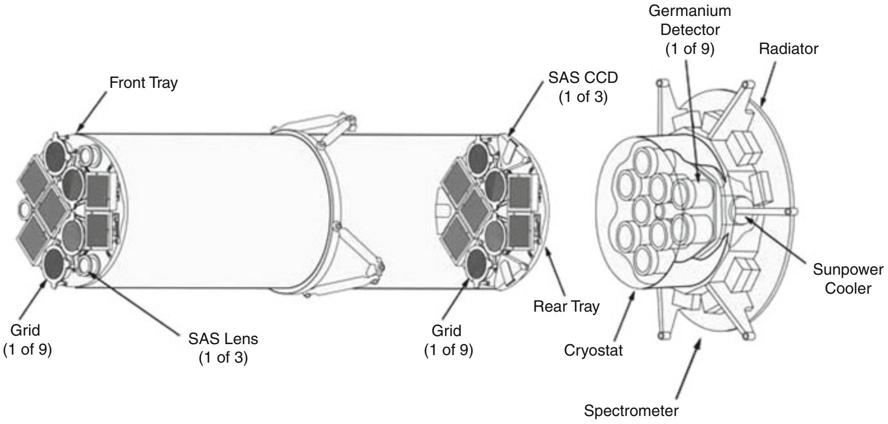

Fig. 13 Perspective of *RHESSI* showing the components necessary for imaging. (After Hurford et al. 2002)

through nuclear reactions of accelerated protons and heavier ions interacting with the ambient thermal ions in the solar atmosphere. Large-volume detectors were required with sufficient sensitivity and fine energy resolution in this difficult energy range where the photon penetrating power becomes so large.

After reviewing the different available techniques for imaging X-rays and gamma rays as discussed in this chapter, it was realized that the only practical method of satisfying these observational requirements within the constraints of NASA's Small Explorer (SMEX) program was to use collimator-based Fourier-transform imaging (Hurford et al., 2002). With only a single instrument involved, it was possible to simply rotate the whole spacecraft in a spin-stabilized configuration to achieve the desired modulation of the incident flux. The resulting RHESSI instrument design is shown in Fig. 13.

RHESSI consisted of two essentially identical sets of nine grids mounted on front and rear grid trays. (All the grids were made of tungsten except for the finest grid pair that was made of molybdenum for ease of etching.) A corresponding set of nine cooled ultrapure germanium detectors was mounted behind the rear grids to measure the modulated X-ray and gamma-ray flux passing through the bi-grid collimators.

The *RHESSI* Imaging Concept

The basic *RHESSI* imaging concept is described in Hurford et al. (2002) and illustrated in Fig. 14. The *RHESSI* instrument encodes imaging information through the RMC technique, in which a set of nine bi-grid collimators rotates with the spacecraft, sweeping possible observing directions across the solar disk and rapidly modulating the detected photon flux in the process. An example of the counting rate time profile for an off-axis source is shown in Fig. 5. Imaging information is encoded in the amplitudes and phases of the X-ray counting rate modulations in the different detectors as the spacecraft rotates at nominally 15 rpm. *RHESSI* is thus termed a

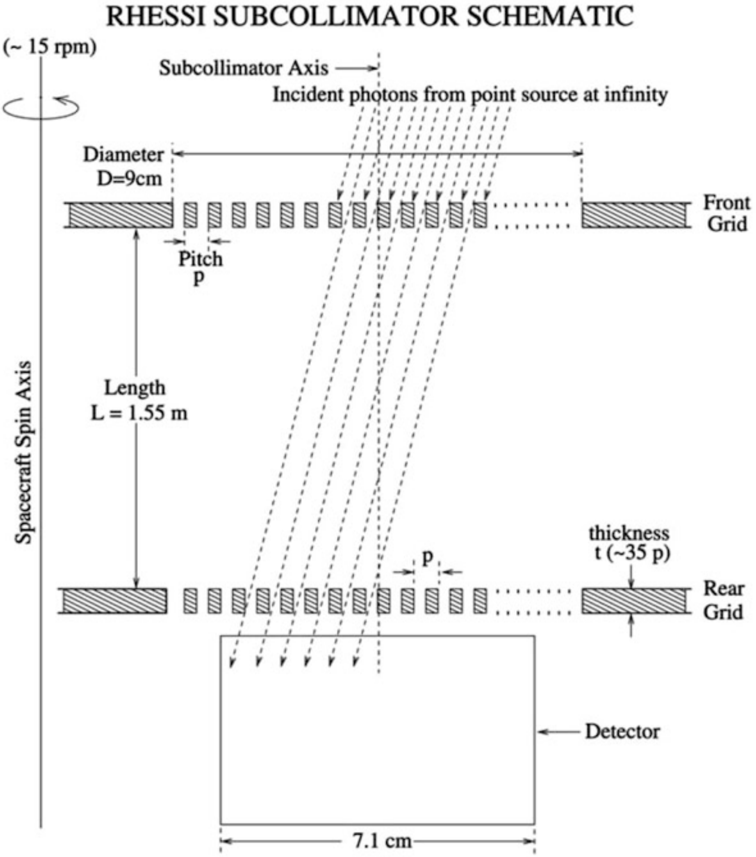

Fig. 14 Geometry of the *RHESSI* imaging process. Light from a distant point source passes through two identical grids, each with a slit/slat pitch of p and separated by a distance L. A detector records a photon only if it passes through both grids; thus, the detected flux depends on the orientation of the grids relative to the source direction. In the spacecraft frame, this direction changes continually due to spacecraft rotation, thus providing a temporally modulated signal that provides information on the source direction. (After Hurford et al. 2002)

"Fourier imager" because it provides imaging information through measurement of the spatial (or, more accurately, angular) Fourier components of the X-ray source(s) that produce these modulated time profiles.

The requisite knowledge of the orientation of the instrument on time scales short compared to the finest modulation time scales was obtained with the solar aspect and roll angle systems. The solar aspect system (SAS) consisted of the three lenses shown in Fig. 13 mounted on the front grid tray to focus optical images of the Sun onto three linear diode arrays (labeled SAS CCDs in the figure) on the rear grid tray. It provides sub-arcsec knowledge of the radial pointing with respect to Sun center. Two optical roll angle systems (RASs, not shown in the figure) were pointed perpendicular to the spin axis to detect multiple stars each spacecraft rotation and provide the necessary roll angle information. The combined SAS and RAS data enables the absolute orientation of the grids to be determined on millisecond time scales and allows X-ray sources to be located on the solar disk to sub-arcsec accuracy (Fivian et al., 2002).

At X-ray energies up to ∼1 MeV, the use of rotating modulation collimators (RMCs) allowed for the measurement of many (over a hundred) spatial frequency (i.e., Fourier) components, covering a broad range of angular size scales from 2 to 180″.

The only other solar X-ray imager using RMCs was the Solar X-ray Telescope (SXT) on the Japanese Hinotori spacecraft, launched in 1981 (Enome, 1983). It consisted of two orthogonal bi-grid modulation collimators on a spacecraft rotating at 4.3 rpm.

Various computational techniques have been devised to generate images of the X-ray sources from telemetered data. These are discussed in detail in Piana et al. (2022). They include methods based directly on the measured counting rates in the nine germanium detectors and those based on the visibilities derived from these counting rates. The former methods include CLEAN, forward fitting, and Pixon; the latter include forward fitting, Bayesian optimization, maximum entropy, etc. One additional capability is to directly generate maps of the flux of the energetic electrons that produced the measured bremsstrahlung X-rays (Piana et al., 2007).

An example of RHESSI's ability to image in X-rays is shown in Fig. 15. The RHESSI contours for two different times and energy ranges show the classic double footpoint hard X-ray sources from precipitating nonthermal electrons accelerated in the flare and lower-energy emission from thermal plasma in a coronal loop-like structure. Note that in the later right-hand image, a coronal hard X-ray source becomes visible as the footpoints fade in brightness.

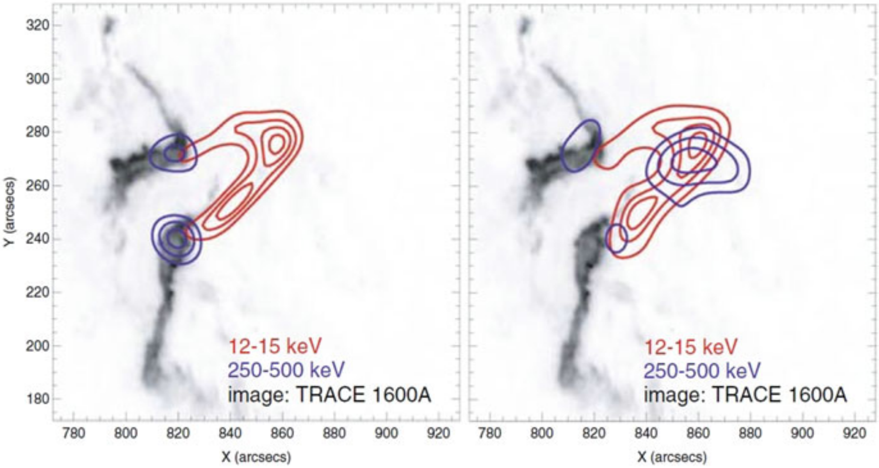

Fig. 15 Contour plots from RHESSI images for a flare on January 20, 2005, superposed on a TRACE UV image. (From Krucker et al. 2008)

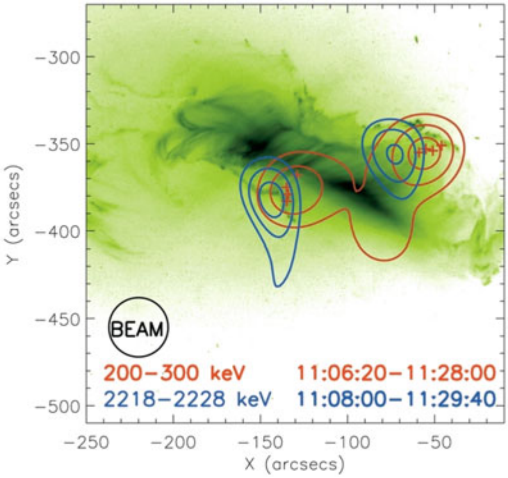

Fig. 16 Contour plots of RHESSI images superposed on a TRACE EUV image. (From Hurford et al. 2006)

As pointed out in Section "Generalities", an advantage of using bi-grid rotating modulation collimators is that the detectors do not have to have any spatial resolution. All the imaging information is encoded in the temporal modulation of the detector counting rates as the spacecraft rotates. This allowed a single cylindrical large-volume (7.1 cm dia. × 8.5 cm long) germanium detector (Smith et al., 2002) to be used behind each collimator. These detectors were able to cover the full energy range required to satisfy both the electron and ion acceleration goals. This was achieved by electronically separating each detector into two segments, a $\sim$1 cm thick front segment, optimized for lower energy photons at energies below a few hundred keV, and a $\sim$7 cm thick rear segment, optimized for higher energy photons up to $>$10 MeV.

The fine ($\sim$1 keV FWHM) X-ray energy resolution of these detectors allowed accurate measurement of the exponentially falling thermal bremsstrahlung spectra and power-law nonthermal spectra that can be as flat as ε^{-2} or as steep as ε^{-10}. The $\sim$2 to 5 keV gamma-ray energy resolution allows all of the nuclear lines, except for the intrinsically narrow neutron capture line at 2.223 MeV, to be fully resolved and line shapes to be determined. Thicker tungsten grids for two of the coarser collimators with angular resolutions of 35 and 183 arcsec allow for modulation at the highest energies and have enabled RHESSI to make the first ever gamma-ray imaging in the neutron capture line (Hurford et al., 2006) shown in Fig. 16.

Single-Grid Imaging Systems

Generalities

Detector technologies continue to improve such that the location of where an X-ray or gamma-ray photon first interacts in the detector plane can be determined with a spatial resolution comparable to the size of the grid slits or slats in a bi-grid system.

Such a sophisticated detector plane can be utilized to modify a bi-grid system into a single-grid system by obviating the need for a rear grid. The resulting single-grid system continues to leverage the principles of bi-grid imaging but with twice the photon throughput compared to the analogous bi-grid system (i.e., $\sim$50% versus $\sim$25%). Furthermore, the modulation shape is now square-wave rather than quasi-triangular, which increases the signal-to-noise ratio.

For a grid with a uniform pitch and held at a fixed orientation relative to the detector, as nominal for a bi-grid collimator, the detector would need to provide spatial information in only 1D (perpendicular to the grid slats). In practice, detectors are commonly able to provide spatial information in 2D, which can be leveraged for further enhancements relative to bi-grid approaches. First, the grid can be of a more complex design, such as having multiple pitches distributed in zones. Second, for approaches based on modulation via rotating, only the single grid needs to be rotated, and the detector plane can stay fixed in orientation.

The finest half-pitch of the grid cannot be smaller than the location resolution of the detector, and thus the achievable angular resolution for imaging is dependent on the wavelength of interest and the detector technology. At X-ray energies, the pixels of modern pixelated solid-state detectors can be large enough (hundreds of microns) to fully absorb an X-ray in a single pixel, yet still fine enough to be matched with a fine grid for high-resolution imaging.

However, at gamma-ray energies, each incident photon can undergo a sequence of interactions due to Compton scattering and pair production, and the spatial separation between partial energy depositions can be on the order of centimeters. Thus, to achieve fine location resolution for where the gamma-ray first interacted with the detector, the detector needs to be able to determine which of the partial energy depositions occurred first. Otherwise, the location resolution of the detector will not be better than the spatial extents of the gamma-ray scatter tracks.

Rotating Modulator (RM)

The rotating modulator (RM), as originally proposed by Durouchoux et al. (1983) as the single-grid analogue of a bi-grid RMC, consists of a uniform-pitch grid rotating in front of a fixed array of identical detectors (Fig. 17).

The location of where a photon interacted in the detector plane is determined simply through which detector absorbed the photon, with the individual detectors not providing any further location information. Accordingly, each detector must be large enough to fully absorb the most energetic photons of interest. At gamma-ray energies, this requirement means that the size scale of the detector, and correspondingly the location resolution of the detector plane, is no smaller than a few centimeters. For a compact gamma-ray instrument, the achievable imaging angular resolution is thus, at best, on the order of 1°.

Nearly three decades later, Louisiana State University built a laboratory prototype RM shown in Fig. 18 called the Lanthanum Bromide-based Rotating Aperture Telescope (LaBRAT; Budden, 2011). The detector plane consisted of 19 cylindrical

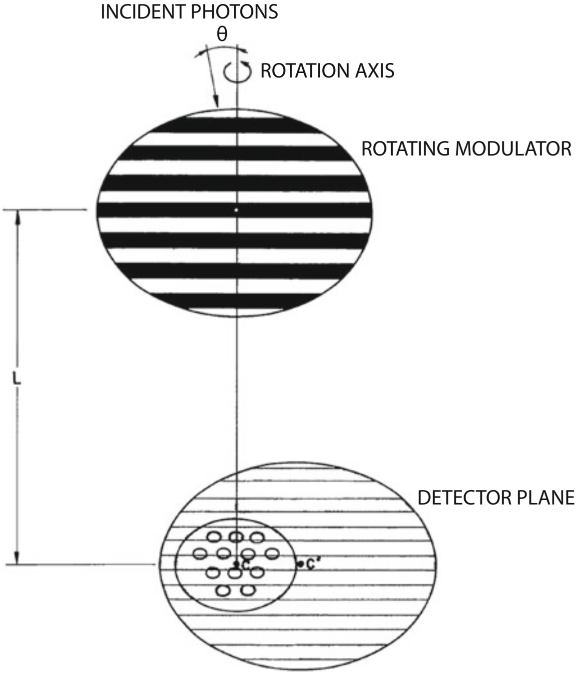

Fig. 17 Illustration of the design for an RM instrument. A rotating grid of coarse slats with a uniform pitch is situated in front of an array of detectors. The location resolution on the detector plane is achieved by knowing which detector absorbed the photon. (From Durouchoux et al. 1983)

scintillators, each 3.8 cm in diameter. The rotating grid consisted of lead slats with a uniform pitch of 7.6 cm, and was situated 1.16 m in front of the detector plane. Thus, the nominal angular resolution was ∼2°. Testing with LaBRAT demonstrated the RM imaging concept, and the developed image-reconstruction technique had success with resolving sources below ∼1°.

As with a bi-grid collimator with a uniform pitch, a given RM is suited for a single angular scale. Although the RM could in principle have multiple grid pitches, the practical size of the grid combined with the required coarse grid pitches limits the number of grid slats. Imaging across a wide range of angular scales would likely require multiple RMs in parallel, spanning a range of grid pitches, especially if good sidelobe response is required. Even so, the limit of ∼1° imaging angular resolution is not adequate for purposes such as solar observations, which desire an angular resolution at least as fine as a few arcseconds.

Multi-Pitch Rotating Modulator (MPRM)

A multi-pitch rotating modulator (MPRM) has been built as part of the *Gamma-Ray Imager/Polarimeter for Solar flares* (*GRIPS*, Duncan et al., 2016) balloon instrument, which had its first Antarctic flight in 2016. The key enabling technology of the MRPM is a detector plane with very high location resolution.

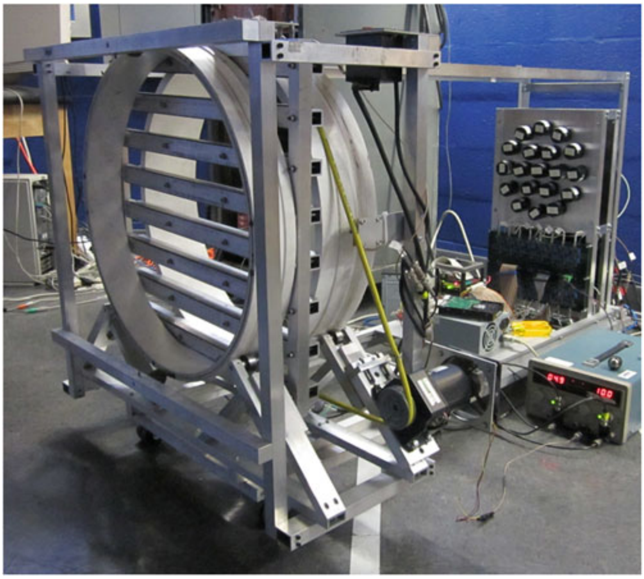

Fig. 18 Photo of the LaBRAT laboratory prototype RM. The rotating grid (left in photo) consisted of lead slats at a uniform pitch, and the detector plane (right in photo) consisted of 19 cylindrical scintillators. The location resolution of the detector plane is achieved by knowing which detector absorbed the photon. (Reproduced from Budden (2011) with permission from B. Budden)

GRIPS utilizes 3D position-sensitive germanium detectors to localize individual energy depositions to $\lesssim$0.5 mm (Fig. 19). Each *GRIPS* detector is of planar geometry (7.5×7.5×1.5 cm), with fine-pitch strip contacts on the cathode face and orthogonally oriented fine-pitch strip contacts on the anode face. An energy deposition in the detector is located in 2D by noting which cathode strip and which anode strip measure the pulse of charge, and is further located in the third dimension by measuring the time difference between the cathode pulse and the anode pulse. It is then possible to separately measure the 3D location of each of the individual energy depositions as a gamma-ray Compton scatters through one or more detectors. Using Compton-scatter kinematics, the initial energy deposition can then be determined. With ~2 orders of magnitude better location resolution than possible with an array of single detectors, the MPRM can achieve high imaging angular resolution and span a wide range of angular scales simultaneously.

The *GRIPS* MPRM is composed of bundles of slats with pitches ranging quasi-continuously from 1 to 13 mm (Fig. 20). To support imaging up to ~10 MeV, the slats are made of a tungsten-copper alloy with a depth of 2.5 cm. Each bundle of slats uses spacers to hold the slats at the correct pitch, and the bundles are held at their ends by the frame. With a grid-detector separation of 8 m, the imaged angular scales range from 12.5 to 162.5 arcsec FWHM. Measuring 13 different angular scales simultaneously results in the excellent sidelobe response as summarized in the "Conclusions" Section.

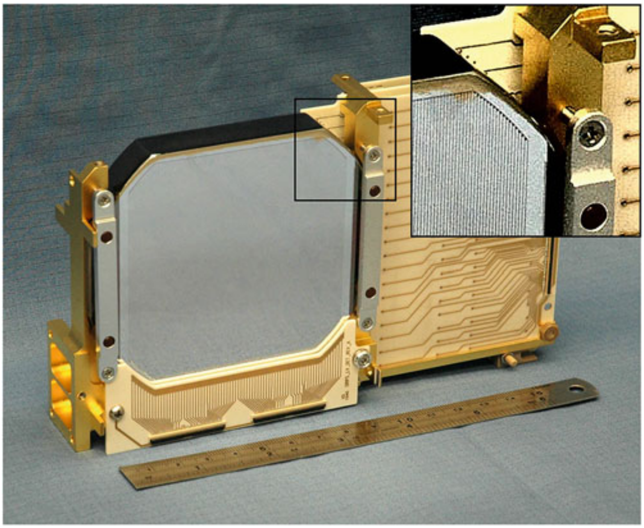

Fig. 19 Photo of a *GRIPS* 3D-position-sensitive germanium detector. The detector dimensions are 7.5 × 7.5 × 1.5 cm, and the visible face shows the strip contacts with a pitch of 0.5 mm. The reverse face (not shown) has strip contacts with the same pitch, but oriented in the perpendicular direction (i.e., approximately horizontal in this photo)

Fig. 20 Photo of part of the *GRIPS* MPRM, showing the variety of grid pitches from 1 mm to 13 mm. The slats are made of tungsten-copper alloy with a depth of 2.5 cm.

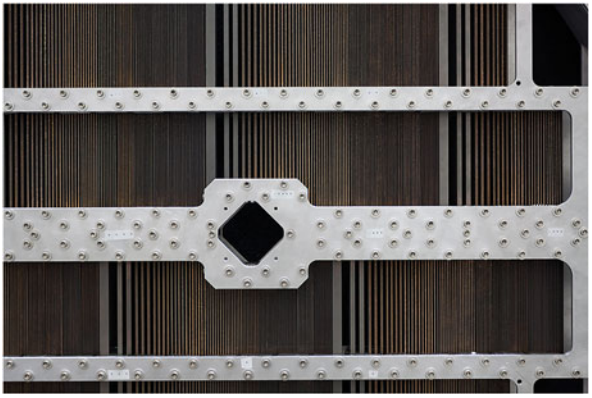

For a given source direction, a given location on the detector is modulated by a grid pitch and grid orientation that varies over time. Figure 21 displays an example back projection from a point source. The image is formed by adding successive probability maps from each captured photon.

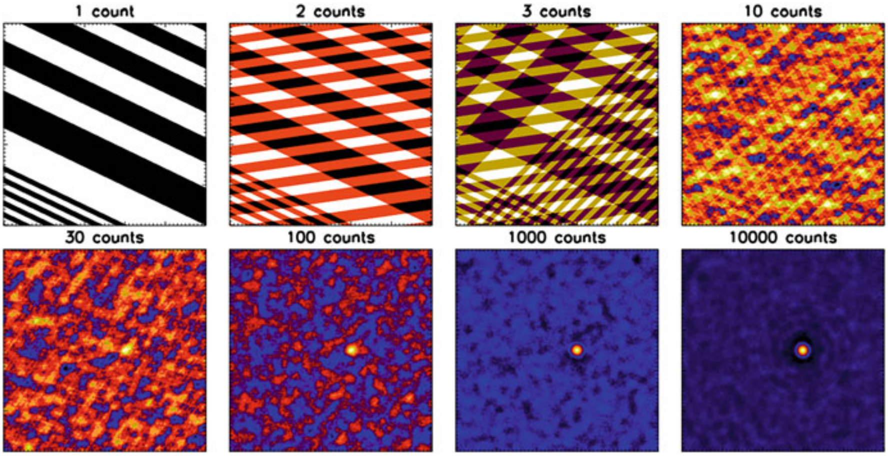

Fig. 21 *GRIPS* back projection of a point source, showing the superposition of successive probability maps of source location. No image deconvolution was applied

Comparison with Coded-Aperture Imaging

Modulation-based imaging via a single, complex grid in front of a position-sensitive detector plane has strong similarities to coded-aperture imaging (see chapter in this volume on "▸ Coded Mask Instruments "). In both cases, the detector plane needs to provide position information that is at least as good as the smallest feature size of the grid/mask, which is set by the desired minimum imageable angular scale. An initial image of the source can be generated by combining the back projections of each photon to the sky based on the transparent parts of the grid/mask. As is typical with indirect imaging, both have limited imaging dynamic range because a bright source in the field of view contributes to the statistical noise of every pixel across the detector plane.

We compare the MPRM with the uniformly redundant array (URA), which is a common form of coded-aperture imaging. Both imaging approaches exhibit very good sidelobe response. The obvious drawback of the MPRM is that it requires the grid to be rotating, and the rotation half-period sets the minimum timescale for producing an image. The URA is preferred when imaging on short timescales is needed, or in implementations where it is not tenable to rotate either the mask alone or the instrument as a whole. An alternative to the MPRM would be a single-grid system with a nonrotating multi-pitch grid that is the analogue of a bi-grid fixed collimator, but then the discretization of measured orientations results in less clean sidelobe response.

Unlike typical applications of URAs for astrophysical observations, high-resolution imaging at gamma-ray energies requires the thickness of the grid/mask to be $\sim 1-2$ orders of magnitude greater than the feature size of the grid/mask. The MPRM can be straightforwardly constructed by stacking slats that can be supported at the ends. In contrast, the URA is not inherently self-supporting, so modifications to the design are needed to be able to support such a large aspect ratio for the features. If the necessary mechanical support results in attenuation or scattering in the energy range of interest, the performance of the URA will be degraded.

In addition, the 1D-like construction of the MRPM lends itself to simpler and less time-consuming characterization and calibration than the 2D URA. The angular scales of the MPRM are also segregated into the individual bundles, as opposed to being highly multiplexed together as in the URA, which allows for straightforward propagation of how fabrication tolerances affect imaging performance.

With respect to producing images, image reconstruction for the MPRM is a laborious process of back projection and deconvolution and/or applying forward-fitting image reconstruction techniques. In contrast, image reconstruction for the URA is computationally straightforward because the illumination pattern on the detector plane can, in principle, be "decoded" by a matrix multiplication. That said, for compact sources, it is possible to extract individual visibilities from just the event list of an MPRM and perform visibility-based analysis, which would not be possible for a URA.

Finally, an important consideration of single-grid imaging is that nonuniform detector background can distort images. The MPRM inherently enables nonuniform detector background to be characterized because each detector pixel is varied rapidly between exposed and not exposed. The URA nominally requires a dark exposure (i.e., looking away from the source) or an inverse exposure (i.e., with an antimask). One could rotate the URA to obtain the benefits of time modulation, but then that would remove one of the key advantages of the URA: not having to rotate.

The MRPM and the URA are both powerful indirect-imaging approaches that can take full advantage of the latest in detector technologies. The choice of one over the other will be driven by the above considerations.

General Grid System Design

Initial ("Optical") design

The optical design is almost purely geometric. Most of the steps are common to all grid-based imaging systems:

1. Start with opaque and thin slat assumptions.
2. Angular scales are given by p/2L, where p is the grid pitch and L the grid separation. Select the minimum grid pitches to define the instrument's best angular resolution and the maximum grid pitches to define the spatial scales beyond which the source will not be properly imaged.
3. Distribute pitches between the two extremes to achieve the desired main-lobe and sidelobe response (uv-plane distribution). When dealing with arrays of collimators each of uniform pitch (e.g., *RHESSI*, STIX, etc.), the weighting can be easily done in software after the observation.

4. Select desired slat thickness. The slats have to be thick enough to be opaque to the incoming radiation. This results in a limited FWHM field of view of ~p/2t, where t is the slat thickness, and a varying slit-to-pitch ratio, s/p, across the field of view. For the six finest *RHESSI* grids, the effective s/p ratio varied from ~60% to ~40% across solar disk, due to shadowing by the finite depth (thickness along optical axis) of the slats (Fig. 6). This was taken into account during imaging reconstruction. The modulation efficiency (a full discussion of which is beyond the scope of this chapter) is diminished by both partial grid opacity and when s/p does not equal 1/2.

The performance of any collimator or mask system is subject to two physical limitations. The first limitation is purely geometrical and is set by a combination of three factors. Specifically, the minimum thickness of the grid is determined by the requirement that the grid be opaque at the maximum energy of interest. This thickness constrains the FOV to an angle given by the ratio of slit width to grid thickness. The slit width in turn is closely tied to the angular resolution (1/2 slit pitch/grid separation). For a collimator of a given length (i.e., grid separation), this combination of factors imposes an unavoidable physics-driven trade-off among angular resolution, FOV, and maximum energy.

The second limitation is diffraction. This sets a lower limit to the energy range since at lower energies the front grid can function as a diffraction grating. This is discussed in Section “Diffraction” with the ultimate limitation on the angular resolution that can be achieved shown in Fig. 22 as functions of energy and grid separation.

Both of these limitations can be relevant in practice. For example, *RHESSI*’s angular resolution above ~1 MeV is limited to 35 arcsec by a requirement that it maintain a 1° FOV. With a 1.55-m-long collimator, *RHESSI* is also prevented from achieving 2.3 arcsec resolution below 4 keV by diffraction.

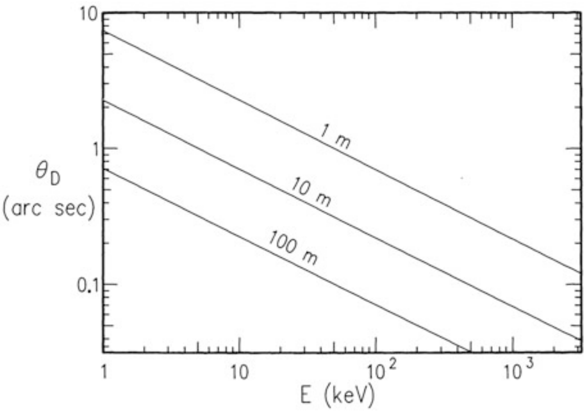

Fig. 22 Diffraction limit on the possible FWHM angular resolution (θ_D) for bi-grid imaging as functions of the X-ray energy (E) and grid-to-grid separation, calculated under the Rayleigh criterion for a single slit. (From Prince et al., 1988)

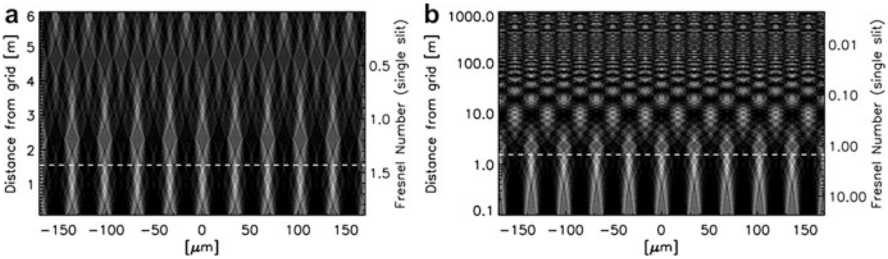

Fig. 23 Diffraction "carpet" at 10 keV for the *RHESSI* finest grid (pitch = 34 microns), assuming an infinite number of slits. The horizontal dashed line corresponds to the 1.55 m distance between the *RHESSI* front and rear grids. (**a**) Linear scale. (**b**) Logarithmic scale

Diffraction

When the wavelength of observations becomes large and the Fresnel number $F = s^2/L\lambda$ becomes $\lesssim 1$ (where s is the slit width and L the grid separation), Fresnel diffraction seriously perturbs the geometric optics assumption ($\lambda = 0$) that is typically used when computing grid responses. The single-slit Fresnel number criterion is akin to constraining the size of the first Fresnel zone $\sim \sqrt{\lambda/L}$ to be smaller than the angular extent of a slit s/L as seen from the opposite grid. The latter typically corresponds to the angular resolution of the collimator. This consideration leads to the best angular resolution that can be achieved as a function of photon energy and grid separation displayed in Fig. 22.

In the diffraction regime, Lindsey (1978) explains in detail the computation of diffraction patterns from one or more grids composed of an infinite series of equally spaced slits (Fig. 23), and Crannell et al. (1991) give the following simplified formula for the factor, D, to multiply the modulation amplitude of a bigrid collimator to account for diffraction: $D = \cos(\pi L h^2 \lambda / p^2)$, where L is the grid separation, p is the grid pitch, h is the harmonic number (1, 2, or 3), and λ is the X-ray photon wavelength. As indicated by the periodicity in this formula, the diffraction pattern indeed repeats itself up to a certain distance where, due to the fact that the grid is not infinite in size, the waves from each slit become isophasic, and the pattern becomes that of a classical grating in the far-field. The transition from one regime to the other occurs at a distance of $\sim g^2/2\lambda$ (where g is the overall grid size), and each regime is well established an order of magnitude below or above that value.

Grid Manufacture

The minimum grating pitch, together with the requirement that the grating be thick enough to stop photons in the desired energy range, drives the choice of manufacturing technique and the material to be used. As a result, several technologies have been used to fabricate the grid or mask "optics" of collimator systems. For coarser grids, mechanical assembly of conventionally machined parts

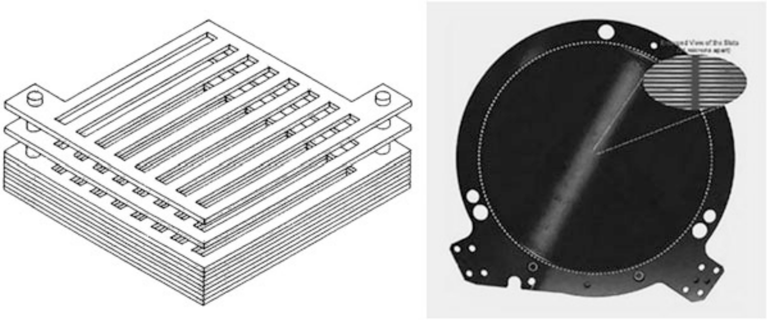

Fig. 24 Grid fabrication techniques. Left: Schematic illustration of stacking photo-etched layers to achieve a thick grid with fine slits. Right: *RHESSI* 9-cm-diameter, 1-mm-thick grid whose slits have a $35\,\mu$m period and a field of view of $\sim 1^\circ$ in a plane perpendicular to the slits and $>20^\circ$ perpendicular to the slits. (From Lin et al. 2002)

is the typical choice. At intermediate pitches, down to ~ 1 mm, electron discharge machining is a viable option (e.g., Crannell et al., 1991). For finer grids, stacking of thin photo-etched foils as shown in Fig. 24 has been used for *RHESSI* (Lin et al., 2002) and for STIX (Krucker et al., 2020) to achieve pitches as fine as $35\,\mu$m in 1-mm-thick tungsten. Finer grids cannot be made with this technique because the smallest features that can be produced by chemical etching are of a similar size to the foil thickness and there is a limit to the availability of thinner tungsten foils.

Lastufka et al. (2020) investigated new fabrication techniques to make the fine grids needed for their proposed Micro Solar-Flare Apparatus (MiSolFA), a compact X-ray imaging spectrometer designed for a small 6U microsatellite. They were successful in producing engineering grids using the LIGA (Lithographie, Galvanoformung, Abformung; or X-ray lithography, electroplating, and molding) fabrication technology. They used a carbon substrate on which they manufactured gold slats with a thickness of more than $200\,\mu$m and a pitch as fine as $15\,\mu$m, far outperforming etching methods. Laser cutting may also be a future relevant technology.

Alignment, Aspect, and Calibration

In this section we provide a broad overview of alignment, aspect, and calibration issues that differ from those used by conventional optical systems.

Bi-grid Collimators

The description of such systems in Section "Bi-grid Systems: Fourier Imagers" assumes an idealized hardware implementation. Such an implementation features "ideal grids" that have negligible thickness but are perfectly opaque at X-ray energies of interest, have a 50% slit-to-pitch ratio, and otherwise have perfect metrology. The position and orientation of the grids are perfectly maintained by the metering structure that is, itself, fixed relative to an aspect system that provides pitch, yaw, and roll information on the direction to the star field or to the solar disk.

The inevitable deviations of the as-built instrument from this ideal state affect the optical performance and so must be determined prior to launch. Directly calibrating the as-built performance using conventional techniques would be problematic since X-ray and gamma-ray beams with the required properties are, in most cases, not available. However, the performance of bi-grid collimators can be well-determined from quasi-two-dimensional characterization of the front and rear grids separately. Specifically, for *RHESSI*, optical scanning of the surfaces of each grid with micron positional accuracy was used to determine the slat pitch, position, orientation, and uniformity. A good estimate of the slit width can also be made from these measurements. In addition, low spatial resolution X-ray transmission measurements as a function of energy and incident angle were made using radioactive sources to determine the slit width, grid thickness, and overall transmission.

These optical and X-ray measurements were combined into a model for each grid from which the transmission as a function of energy and incident angle can be reliably inferred. These combined transmission profiles of the front and rear grids as a function of position then provide the basis for a realistic estimate of the imager response as a function of energy and incident angle. The experience with *RHESSI* showed that redundant determinations were good at the 2% level.

The interpretation of the grid pair data can be done using CAD techniques. In practice, a much more efficient approach is to express the response (as a function of energy and incident angle) in terms of just three parameters – the average transmission, the amplitude, and phase of the periodic response as a function of incident angle. These three parameters fully describe the relevant response and vary smoothly with energy and incident angle.

Since the parameters can be analytically adapted to the as-built performance, the calibration is based on knowledge of the as-built hardware, as opposed to requiring that the hardware meet high metrology requirements. Furthermore, this knowledge can be obtained after the fact and applied to previous observations. Thus, in many cases, post facto knowledge of the in-flight metrology can be used to fully compensate for degradation caused by imperfect or misaligned grids and other practical considerations.

An example of this knowledge vs. control dichotomy is the relative twist of the front and rear grids. In fact, this need only to be aligned to a precision given by the ratio of grid slit to grid diameter, rather than grid slit to separation. Similarly, if the elements of the aspect system are built into the grids or the grid mounts as was the case for *RHESSI* (e.g., Zehnder et al., 2003), then mechanical flexure in the overall metering structure is equivalent to a variation in pointing and is reflected in the aspect solution. With photon tagging, short integration times, and a high-cadence aspect system, such variations can be fully compensated for during analysis.

In practice, the knowledge vs. control trade-off with *RHESSI* enabled observations with ∼arcsecond resolution to be obtained with a metering structure that was stable to ∼arcminutes and with pointing stable to ∼a degree.

One distinguishing feature of bi-grid systems is that the transverse location of the detector need only be located to an accuracy better than the grid size, not the grid-aperture size. This is particularly useful since it supports late stage integration of the detector and grid optics. The distance of the detector from the rear grid is generally not critical, unlike the focus requirements of a focusing imager.

The alignment requirements for multi-grid collimators are much more severe than for bi-grid collimators since the intermediate grids must be positioned and maintained to a precision that is small compared to the grid pitch. This requirement was met, however, by the HXIS instrument on *SMM* with $\sim 25\,\mu$ m grid apertures (van Beek et al., 1980).

Systems with 2D Detectors

The significance of internal alignment and tolerance issues depends on the type of mask or collimator system employed. For mask systems that include detectors with two-dimensional spatial capability, the primary requirement is that the relative positions of the mask and detector be known in inertial coordinates to an accuracy small compared to the angular resolution. This must be achieved on timescales that are longer than the integration time. The requirement can be met if both the metering structure and pointing platform are stable. Alternatively, as with *RHESSI*, one can trade mechanical and pointing stability for data rate by using photon tagging, short binning times, and a high-cadence aspect system.

The fact that photons are received in various areas of the spatially sensitive detectors (further reinforced by any jitter the collimator is subject to) ensures that no single source location is disadvantaged. This is in contrast to RMC systems that have limited ability to image a source that is within a pitch angular separation from the spin axis. Also, every detector pixel “sees” all angular scales, and this eases some calibration issues. For example, in a *RHESSI*-like bi-grid, each detector is associated with a particular angular scale, and inter-detector sensitivity errors lead to certain spatial scales being under- or overemphasized with respect to the others.

Conclusions

Grids and masks have provided the basis for X-ray and gamma-ray imaging since the 1960s (Bradt et al., 1968, 1992) (Also see the list of missions found at https://universe.gsfc.nasa.gov/archive/cai/coded_inss.html.). Table 1 compares the capabilities of imagers using the three different schemes: single grid, bi-grid, and multi-grid. Table 2 summarizes the characteristics of a representative set of instruments that have made observations either on spacecraft or on high-altitude balloons, with Fig. 25 displaying a few point spread functions for comparison. Their capabilities have grown as grid and detector technologies have improved.

The different techniques that have been employed have both advantages along with significant disadvantages. The design requirement that the detector area be comparable to that of the grid or mask makes it much more difficult to reduce

Table 1 Qualitative comparison between imaging schemes. Note that rotation-based imaging instruments typically have minimal image accumulations of half a spin period. Color code: blue, best or special mention; green, very good, current cutting edge; yellow, standard or adequate for solar work; orange, below preferred standard for solar applications; red, avoid unless irrelevant!

Imaging type	Fixed/ rotating	Angular resolution	Sidelobe levels	FOV	Temp. res. (imaging)	Sensitivity or Aeff	Pixelized detectors?	Other notes
URA	Fixed	$\sim \frac{c_{\min}}{L}$	very good	$\gtrsim 1°$, with vignetting	statistics-limited	$\sim \frac{1}{2} A_{\mathrm{det}}$	required	challenging to fabricate and to calibrate
Single grid (Multi-pitch)	Rotating	$\sim \frac{p_{\min}}{2L}$	very good	$\gtrsim 1°$	$\geq \frac{1}{2}$period	$\sim \frac{1}{2} A_{\mathrm{det}}$	required	PSF ∼fixed
	Fixed		good		statistics-limited			
Bi-grid (One or two SC(s) per pitch)	Rotating	$\sim \frac{p_{\min}}{2L}$	very good	$\gtrsim 1°$	$\geq \frac{1}{2}$period	$\sim \frac{1}{4} A_{\mathrm{det}}$	not required	"Visibilities"; PSF weighted post-facto in S/W;
	Fixed (cos & sine SCs)		good		statistics-limited			
	Fixed (moiré)						only coarse required	moiré: visibilities robustly formed
Multi-grid	Fixed	$\sim \frac{p_{\min}}{2L}$	none!	$N_{SC} \approx \left(\frac{\mathrm{FOV}}{\mathrm{ang.res.}}\right)^2$	statistics-limited	very small	required	
Focusing Optics	Fixed	5″	on-axis off-axis	∼10′	statistics-limited	A_{optics} Low background	required	HXRs only

Where detector pixelization is required, it is typically at the level of half the (finest) grid pitch $p_{\min}$

The minimum size of a URA feature ($c_{\min}$) is typically half the minimum pitch of a periodic grid ($p_{\min}$)

The bi-grid row assumes the use of multiple collimators to measure a range of spatial frequencies

Table 2 Past instruments. Most nominally require information about all detected photons to be downlinked, although some significant on-board data compression schemes have been used when needed to reduce the telemetered data volume (e.g., STIX on *Solar Orbiter*). Instruments using URAs and random masks have been added for reference. (Adapted from Hurford 2010)

Mission/instrument	Description	Ang. res.	FOV	Energy band [keV]	Aeff [cm^2]	Misc. notes
Ariel/B (1974–1980) Villa et al. (1976)	scanner	$0.75''$	survey	0.9 to 18	$\approx$290	
SMM/HXIS (1980) van Beek et al. (1980)	multi-grid direct img	$8''$	solar	3.5 to 30	0.07	
Hinotori SXT (1981) Enome (1983)	2 RMCs	$30''$ & $38''$	solar flares	17 to 40		
Yohkoh/HXT (1991–2001) Kosugi et al. (1991)	64 bi-grid collimators (sine & cosine)	$8''$	solar flares	15 to 100	70	
HEIDI (1993 balloon) Crannell et al. (1991)	2 RMCs	$11''$ & $25''$	1°	$\leq$20 to 700	32	
HETE-2/WXM (2000–2008) Kawai et al. (1999)	two 1-D random masks	$\approx 10'$	burst location	2 to 25	350	
INTEGRAL/IBIS (2002–present) Ubertini et al. (2003)	URA	$12'$	source identification	15 to 10,000	2500	
RHESSI (2002–2018) Lin et al. (2002)	9 RMCs	$2.3''$	1° solar	3 to 17,000	50 keV:50 2.2 MeV:3	
Swift/BAT (2004–present) Barthelmy et al. (2005)	URA	$17'$	burst location	15 to 150	5200	
GRIPS (2016 balloon) Duncan et al. (2016)	Rotating MPRM mask	$12.5''$	1° (flares)	20 to 10,000	50 keV:90 2.2 MeV:13	MDP $\approx$3%
Solar Orbiter/STIX (2021–present) Krucker et al. (2020)	30 bi-grid collimators	$7.1''$	2° (flares)	3 to 150	6	100-byte images
ASO-S/HXI (launch in 2022) Zhang et al. (2019)	91 bi-grid collimators (sine & cosine)	$6''$	$40'$	30 to 200	$\approx$96	

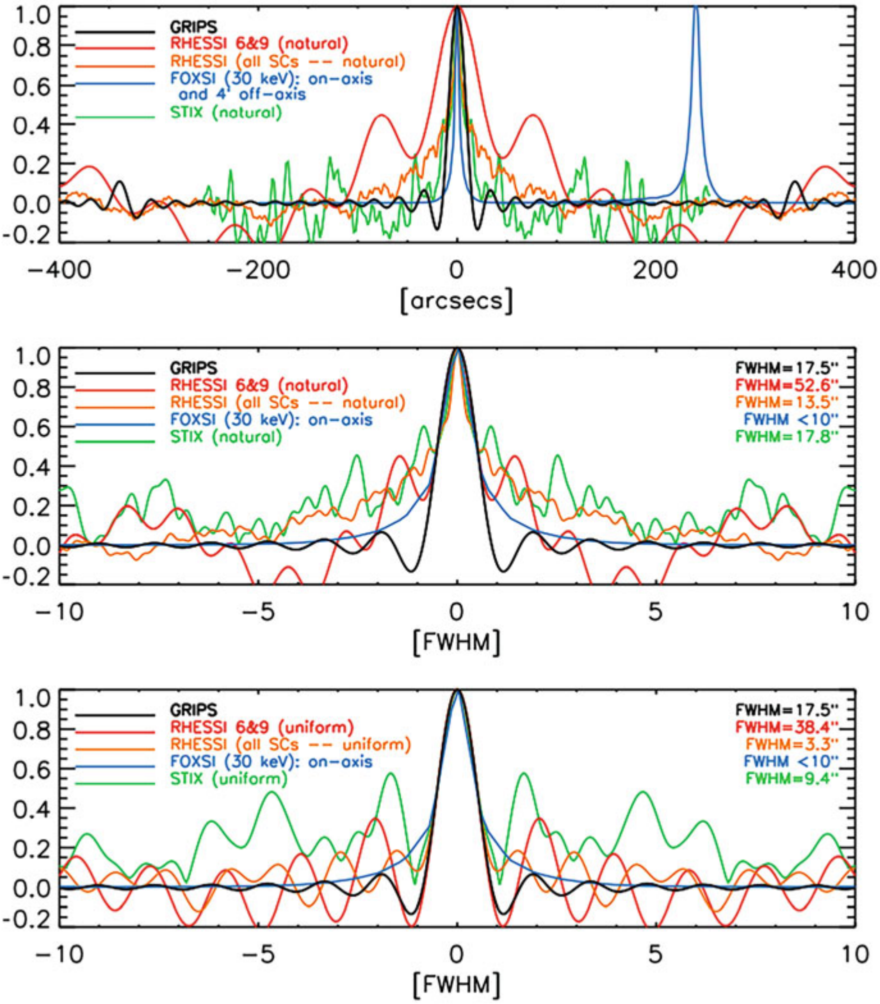

Fig. 25 Point spread functions of *GRIPS*, *RHESSI*, *Solar Orbiter*/STIX, and *FOXSI* (Focusing Optics X-ray Spectroscopic Imager Krucker et al., 2013). The *RHESSI* subcollimators #6 and #9 were the only ones thick enough to modulate gamma rays at energies above ∼1 MeV, and hence, this combination is shown separately. *Top:* Natural weighting (all visibilities are weighted equally) and abscissa in arcsecs. *Middle:* Natural weighting and abscissa in units of the FWHM of the main lobe. *Bottom:* Uniform weighting (where individual visibilities are weighted such as to preserve the density of uv points in Fourier space) and abscissa in units of the FWHM of the main lobe

background for applications that require high sensitivity. Sensitivity is further affected since the telescope mask or collimator intentionally blocks between about a half to three quarters of the incident photon flux. In source-limited situations where background is not an issue, the ability to detect weak sources in the presence of strong ones is limited by the fact that all sources contribute noise to the detection of each source component. Image quality is also significantly constrained for complex sources (single-mask and bi-grid systems).

In recent years, masks and collimators have been partially supplanted by technical developments in grazing-incidence optics for low-energy applications that require only intermediate resolution and narrow FOVs. In such contexts, focusing optics has a commanding advantage where sensitivity and background rejection are the main drivers or where morphologically complex sources need be imaged. Nevertheless, there will continue to be many applications where mask and grid-based imaging is appropriate. As we have seen, the technique can be adapted to platforms which are three-axis stabilized, rotating, or unstably pointed (as with balloons). It can also be implemented in a wide range of size scales, from compact designs of a few centimeters in scale to configurations requiring extended booms on scales of meters. It can provide angular resolutions from seconds of arc to degrees over FOVs from $\sim 1^\circ \times 1^\circ$ to ~ 1 sr (see also the Hemispherical Rotational Modulation Collimator Imaging System; Kim et al., 2019). For a given instrument, the same "optics" can be used over a wide range of energies, a feature that greatly aids co-location of images and imaging spectroscopy. Therefore, in applications where either compactness, low mass, wide FOV, high angular resolution, or high-energy response is required, masks, grids, and collimators will continue to provide the imaging technique of choice.

References

S.D. Barthelmy, L.M. Barbier, J.R. Cummings, E.E. Fenimore, N. Gehrels, D. Hullinger, H.A. Krimm, C.B. Markwardt, D.M. Palmer, A. Parsons, G. Sato, M. Suzuki, T. Takahashi, M. Tashiro, J. Tueller, Space Sci. Rev. **120**, 143 (2005)

H. Bradt, G. Garmire, M. Oda, G. Spada, B.V. Sreekantan, P. Gorenstein, H. Gursky, Space Sci. Rev. **8**, 471 (1968)

H.V.D. Bradt, T. Ohashi, K.A. Pounds, ARAA **30**, 391 (1992)

B. Budden, PhD thesis, Louisiana State University, 2011

C.J. Crannell, B.R. Dennis, J.P. Norris, L.E. Orwig, E.J. Schmahl, F.L. Lang, R. Starr, M.E. Greene, G.J. Hurford, W.N. Johnson, K.S. Wood, in *AIAA International Balloon Conference*, Albuquerque, vol. AIM-91-3653-CP, 1991

N. Duncan, P. Saint-Hilaire, A.Y. Shih, G.J. Hurford, H.M. Bain, M. Amman, B.A. Mochizuki, J. Hoberman, J. Olson, B.A. Maruca, N.M. Godbole, D.M. Smith, J. Sample, N.A. Kelley, A. Zoglauer, A. Caspi, P. Kaufmann, S. Boggs, R.P. Lin, in *Society of Photo-Optical Instrumentation Engineers (SPIE) Conference Series*, ed. by J.-W.A. den Herder, T. Takahashi, M. Bautz. Space Telescopes and Instrumentation 2016: Ultraviolet to Gamma Ray, vol. 9905 (2016), p. 99052Q

P. Durouchoux, H. Hudson, J. Matteson, G. Hurford, K. Hurley, E. Orsal, Astron. Astrophys. **120**, 150 (1983)

S. Enome, Adv. Space Res. **2**, 201 (1983)

M. Fivian, R. Hemmeck, A. McHedlishvili, A. Zehnder, Sol. Phys. **210**, 87 (2002)

G.J. Hurford, ISSI Sci. Rep. Ser. **9**, 223 (2010)

G.J. Hurford, S. Krucker, R.P. Lin, R.A. Schwartz, G.H. Share, D.M. Smith, Astrophys. J. Lett. **644**, L93 (2006)

G.J. Hurford, E.J. Schmahl, R.A. Schwartz, A.J. Conway, M.J. Aschwanden, A. Csillaghy, B.R. Dennis, C. Johns-Krull, S. Krucker, R.P. Lin, J. McTiernan, T.R. Metcalf, J. Sato, D.M. Smith, Sol. Phys. **210**, 61 (2002)

N. Kawai, M. Matsuoka, A. Yoshida, Y. Shirasaki, M. Namiki, K. Takagishi, M. Yamauchi, I. Hatsukade, E.E. Fenimore, M. Galassi, Astron. Astrophys. Suppl. **138**, 563 (1999)

H.S. Kim, M. Na, J.G. Ok, G. Kim, S.-J. Ye, IEEE Trans. Nucl. Sci. **66**, 2114 (2019)

T. Kosugi, K. Makishima, T. Murakami, T. Sakao, T. Dotani, M. Inda, K. Kai, S. Masuda, H. Nakajima, Y. Ogawara, M. Sawa, K. Shibasaki, Sol. Phys. **136**, 17 (1991)

S. Krucker, S. Christe, L. Glesener, S. Ishikawa, B. Ramsey, M. Gubarev, S. Saito, T. Takahashi, S. Watanabe, H. Tajima, T. Tanaka, P. Turin, D. Glaser, J. Fermin, R.P. Lin, in *Society of Photo-Optical Instrumentation Engineers (SPIE) Conference Series*, ed. by S. Fineschi, J. Fennelly. Solar Physics and Space Weather Instrumentation V, vol. 8862 (2013), p. 88620R

S. Krucker, G.J. Hurford, O. Grimm, S. Kögl, H.P. Gröbelbauer, L. Etesi, D. Casadei, A. Csillaghy, A.O. Benz, N.G. Arnold, F. Molendini, P. Orleanski, D. Schori, H. Xiao, M. Kuhar, N. Hochmuth, S. Felix, F. Schramka, S. Marcin, S. Kobler, L. Iseli, M. Dreier, H.J. Wiehl, L. Kleint, M. Battaglia, E. Lastufka, H. Sathiapal, K. Lapadula, M. Bednarzik, G. Birrer, S. Stutz, C. Wild, F. Marone, K.R. Skup, A. Cichocki, K. Ber, K. Rutkowski, W. Bujwan, G. Juchnikowski, M. Winkler, M. Darmetko, M. Michalska, K. Seweryn, A. Białek, P. Osica, J. Sylwester, M. Kowalinski, D. Ścisłowski, M. Siarkowski, M. Steślicki, T. Mrozek, P. Podgórski, A. Meuris, O. Limousin, O. Gevin, I. Le Mer, S. Brun, A. Strugarek, N. Vilmer, S. Musset, M. Maksimović, F. Fárník, Z. Kozáček, J. Kašparová, G. Mann, H. Önel, A. Warmuth, J. Rendtel, J. Anderson, S. Bauer, F. Dionies, J. Paschke, D. Plüschke, M. Woche, F. Schuller, A.M. Veronig, E.C.M. Dickson, P.T. Gallagher, S.A. Maloney, D.S. Bloomfield, M. Piana, A.M. Massone, F. Benvenuto, P. Massa, R.A. Schwartz, B.R. Dennis, H.F. van Beek, J. Rodríguez-Pacheco, R.P. Lin, Astron. Astrophys. **642**, A15 (2020)

S. Krucker, G.J. Hurford, A.L. MacKinnon, A.Y. Shih, R.P. Lin, Astrophys. J. Lett. **678**, L63 (2008)

E. Lastufka, D. Casadei, G. Hurford, M. Kuhar, G. Torre, S. Krucker, Adv. Space Res. **66**, 10 (2020)

R.P. Lin, B.R. Dennis, G.J. Hurford, D.M. Smith, A. Zehnder, P.R. Harvey, D.W. Curtis, D. Pankow, P. Turin, M. Bester, A. Csillaghy, M. Lewis, N. Madden, H.F. van Beek, M. Appleby, T. Raudorf, J. McTiernan, R. Ramaty, E. Schmahl, R. Schwartz, S. Krucker, R. Abiad, T. Quinn, P. Berg, M. Hashii, R. Sterling, R. Jackson, R. Pratt, R.D. Campbell, D. Malone, D. Landis, C.P. Barrington-Leigh, S. Slassi-Sennou, C. Cork, D. Clark, D. Amato, L. Orwig, R. Boyle, I.S. Banks, K. Shirey, A.K. Tolbert, D. Zarro, F. Snow, K. Thomsen, R. Henneck, A. McHedlishvili, P. Ming, M. Fivian, J. Jordan, R. Wanner, J. Crubb, J. Preble, M. Matranga, A. Benz, H. Hudson, R.C. Canfield, G.D. Holman, C. Crannell, T. Kosugi, A.G. Emslie, N. Vilmer, J.C. Brown, C. Johns-Krull, M. Aschwanden, T. Metcalf, A. Conway, Sol. Phys. **210**, 3 (2002)

C.A. Lindsey, J. Opt. Soc. Am. (1917–1983) **68**, 1708 (1978)

K. Makishima, T. Murakami, J. Nishimura, M. Oda, Y. Ogawara, Y. Tawara, S. Miyamoto, COSPAR, 20th Plenary Meeting, vol. 20, 1977

P. Massa, A.F. Battaglia, A. Volpara, H. Collier, G.J. Hurford, M. Kuhar, E. Perracchione, S. Garbarino, A.M. Massone, F. Benvenuto, F. Schuller, A. Warmuth, E.C.M. Dickson, H. Xiao, S.A. Maloney, D.F. Ryan, M. Piana, S. Krucker (2022). arXiv e-prints, arXiv:2202.09334

S. Masuda, in *Multi-Wavelength Observations of Coronal Structure and Dynamics*, ed. by P.C.H. Martens, D. Cauffman, vol. 10 (2002), pp. 351–359

L. Mertz, in *Modern Optics*, ed. by J. Fox (1967), p. 787

M. Oda, Appl. Opt. **4**, 143 (1965)

M. Piana, A.M. Massone, G.J. Hurford, M. Prato, A.G. Emslie, E.P. Kontar, R.A. Schwartz, Astrophys. J. **665**, 846 (2007)

M. Piana, A.G. Emslie, A.M. Massone, B.R. Dennis, *Hard X-ray Imaging of Solar Flares* (Springer, 2022), p. 164

T.A. Prince, G.J. Hurford, H.S. Hudson, C.J. Crannell, Sol. Phys. **118**, 269 (1988)

B.D. Ramsey, R.A. Austin, R. Decher, Instrumentation for x-ray astronomy, NASA Marshall Space Flight Center Report, 1993

E.J. Schmahl, G.J. Hurford, Sol. Phys. **210**, 273 (2002)

H.W. Schnopper, R.I. Thompson, S. Watt, Space Sci. Rev. **8**, 534 (1968)

D.M. Smith, R.P. Lin, P. Turin, D.W. Curtis, J.H. Primbsch, R.D. Campbell, R. Abiad, P. Schroeder, C.P. Cork, E.L. Hull, D.A. Land is, N.W. Madden, D. Malone, R.H. Pehl, T. Raudorf, P. Sangsingkeow, R. Boyle, I.S. Banks, K. Shirey, R. Schwartz, Sol. Phys. **210**, 33 (2002)

W. Soller, Phys. Rev. **24**, 158 (1924)

P. Ubertini, F. Lebrun, G. Di Cocco, A. Bazzano, A.J. Bird, K. Broenstad, A. Goldwurm, G. La Rosa, C. Labanti, P. Laurent, I.F. Mirabel, E.M. Quadrini, B. Ramsey, V. Reglero, L. Sabau, B. Sacco, R. Staubert, L. Vigroux, M.C. Weisskopf, A.A. Zdziarski, Astron. Astrophys. **411**, L131 (2003)

H.F. van Beek, C. de Jager, A. Schadee, Z. Svestka, A. Boelee, A. Duijveman, M. Galama, R. Hoekstra, P. Hoyng, R. Fryer, G.M. Simnett, J.P. Imhof, H. LaFleur, H.V.A.M. Maseland, W.M. Mels, J. Schrijver, J.J.M. van der Laan, P. van Rens, W. van Tend, F. Werkhoven, A.P. Willmore, J.W.G. Wilson, M.E. Machado, W. Zandee, Astrophys. J. Lett. **244**, L157 (1981)

H.F. van Beek, P. Hoyng, B. Lafleur, G.M. Simnett, Sol. Phys. **65**, 39 (1980)

G. Villa, C.G. Page, M.J.L. Turner, B.A. Cooke, M.J. Ricketts, K.A. Pounds, D.J. Adams, Mon. Not. R. Astron. Soc. **176**, 609 (1976)

A. Zehnder, J. Bialkowski, F. Burri, M. Fivian, R. Henneck, A. Mchedlishvili, P. Ming, J. Welte, K. Thomsen, D. Clark, B.R. Dennis, G.J. Hurford, D.W. Curtis, P.R. Harvey, D.H. Pankow, in *Society of Photo-Optical Instrumentation Engineers (SPIE) Conference Series*, ed. by S.L. Keil, S.V. Avakyan. Innovative Telescopes and Instrumentation for Solar Astrophysics, vol. 4853 (2003), pp. 41–59

Z. Zhang, D.-Y. Chen, J. Wu, J. Chang, Y.-M. Hu, Y. Su, Y. Zhang, J.-P. Wang, Y.-M. Liang, T. Ma, J.-H. Guo, M.-S. Cai, Y.-Q. Zhang, Y.-Y. Huang, X.-Y. Peng, Z.-B. Tang, X. Zhao, H.-H. Zhou, L.-G. Wang, J.-X. Song, M. Ma, G.-Z. Xu, J.-F. Yang, D. Lu, Y.-H. He, J.-Y. Tao, X.-L. Ma, B.-G. Lv, Y.-P. Bai, C.-X. Cao, Y. Huang, W.-Q. Gan, Res. Astron. Astrophys. **19**, 160 (2019)